nature photonics

LETTERS

PUBLISHED ONLINE: 19 APRIL 2009 | DOI: 10.1038/NPHOTON.2009.46

Controlling the near-field oscillations of loaded plasmonic nanoantennas

M. Schnell[1], A. García-Etxarri[2], A. J. Huber[1,3], K. Crozier[4], J. Aizpurua[2] and R. Hillenbrand[1,3]*

Optical and infrared antennas[1–6] enable a variety of cutting-edge applications ranging from nanoscale photodetectors[7] to highly sensitive biosensors[8]. All these applications critically rely on the optical near-field interaction between the antenna and its 'load' (biomolecules or semiconductors). However, it is largely unexplored how antenna loading affects the near-field response. Here, we use scattering-type near-field microscopy to monitor the evolution of the near-field oscillations of infrared gap antennas progressively loaded with metallic bridges of varying size. Our results provide direct experimental evidence that the local near-field amplitude and phase can be controlled by antenna loading, in excellent agreement with numerical calculations. By modelling the antenna loads as nanocapacitors and nanoinductors[9–11], we show that the change of near-field patterns induced by the load can be understood within the framework of circuit theory. Targeted antenna loading provides an excellent means of engineering complex antenna configurations in coherent control applications[12], adaptive nano-optics[13] and metamaterials[14].

Optical and infrared antennas based on metal nanostructures allow for efficient conversion of propagating light into nanoscale confined and strongly enhanced optical fields, and vice versa[1–5,15]. Antennas consisting of adjacent metallic segments (that is, nanorods) separated by a nanoscopic gap (gap antennas)[1,3,4,7,8,16,17] are particularly efficient. The near-field coupling across the gap can generate extremely strong and localized fields, which are essential for applications such as single-molecule surface-enhanced Raman spectroscopy (SERS)[8] or extreme-ultraviolet (EUV) generation[16]. However, the antenna response is very sensitive to small environmental changes at the gap[18–20]. Thus, the presence of molecules or semiconductors in the gap (as is usually the case in spectroscopy or detector applications) can dramatically affect the antenna's far-field optical response with the possibility of degrading the antenna performance. On the other hand, we can take advantage of this effect for versatile tuning of the antenna response. Recently, Alù and Engheta[9,10] described this possibility in terms of antenna loading, a concept adapted from radio-frequency (RF) technology. Following the RF design rules, it has been theoretically demonstrated that the scattering response and resonance frequency of optical antennas can be tuned by loading the antenna gap with either metals or dielectrics acting as inductors or capacitors, respectively. In this Letter, we present an experimental study of how loading of antenna gaps affects the near-field response using scattering-type scanning near-field optical microscopy (s-SNOM)[21]. We provide direct experimental evidence that the local near-field amplitude and phase response can be controlled by antenna loading.

Our experiments were performed with antennas based on gold nanorods designed for fundamental dipolar resonance at mid-infrared frequencies. The rods ($1{,}550 \times 230 \times 60$ nm) were fabricated on a silicon substrate by electron-beam lithography and show a far-field resonance at a wavelength of $\lambda = 9.6$ μm (ref. 2). Note that the antenna length is significantly shorter than $\lambda/2$ due to dielectric screening by the substrate, the large width of the antenna compared to its length and plasmonic effects[15,22]. To study how the progressive loading of an antenna gap affects the near-field distribution, we used focused ion beam (FIB) milling to prepare gaps of different shapes and sizes at the centre of the rods. Using a transmission-mode s-SNOM[21,23] operating at a wavelength of $\lambda = 9.6$ μm (Fig. 1), near-field amplitude and phase images of the rods were recorded.

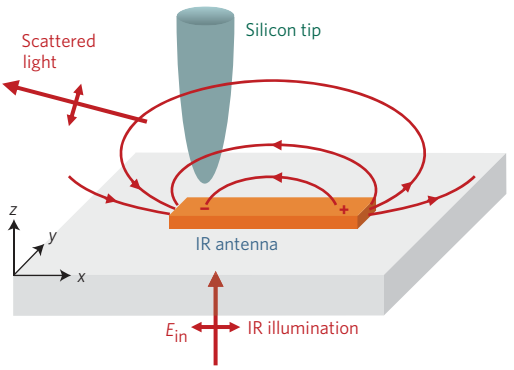

Figure 1 | Mapping the near-field distribution of optical antennas with a transmission-mode s-SNOM. The antenna is illuminated from below through a transparent substrate. While scanning the sample, the near fields of the antenna are scattered by the tip and recorded interferometrically, yielding infrared amplitude and phase images simultaneously to topography.

In a first experiment with well established dipole antennas[2] we demonstrated that transmission-mode s-SNOM equipped with dielectric tips allows for reliable mapping of antenna near-field modes. Figure 2a shows the infrared near-field amplitude and phase images of a continuous (unmodified) nanorod. The images reveal strong-amplitude signals at the rod extremities and a phase jump of about 180° at the rod centre, providing direct experimental evidence of an anti-phase field oscillation as expected for the dipolar near-field mode. To analyse the image contrast, we performed numerical calculations of the x- and z-components of the near-field distribution of a 1,550-nm-long nanorod in resonance at a wavelength of 9.6 μm (see Supplementary Fig. S1). Comparison with the experimental data clearly shows that the amplitude and phase of the z-component, $|E_z|$ and φ_z, are probed[24] (Fig. 2a, bottom).

In Fig. 2d we study a nanorod that was fully cut in its centre, representing an unloaded gap antenna. The topography image clearly reveals the two closely spaced segments separated by a

[1]Nanooptics Laboratory, CIC nanoGUNE, 20018 Donostia – San Sebastián, Spain, [2]Centro de Física de Materiales (CSIC-UPV/EHU) and Donostia International Physics Center (DIPC), 20018 Donostia – San Sebastián, Spain, [3]Nano-Photonics Group, Max-Planck-Institut für Biochemie, 82152 Martinsried and Center for NanoScience (CeNS), Munich, Germany, [4]Harvard University, Cambridge, Massachusetts 02138, USA. *e-mail: r.hillenbrand@nanogune.eu

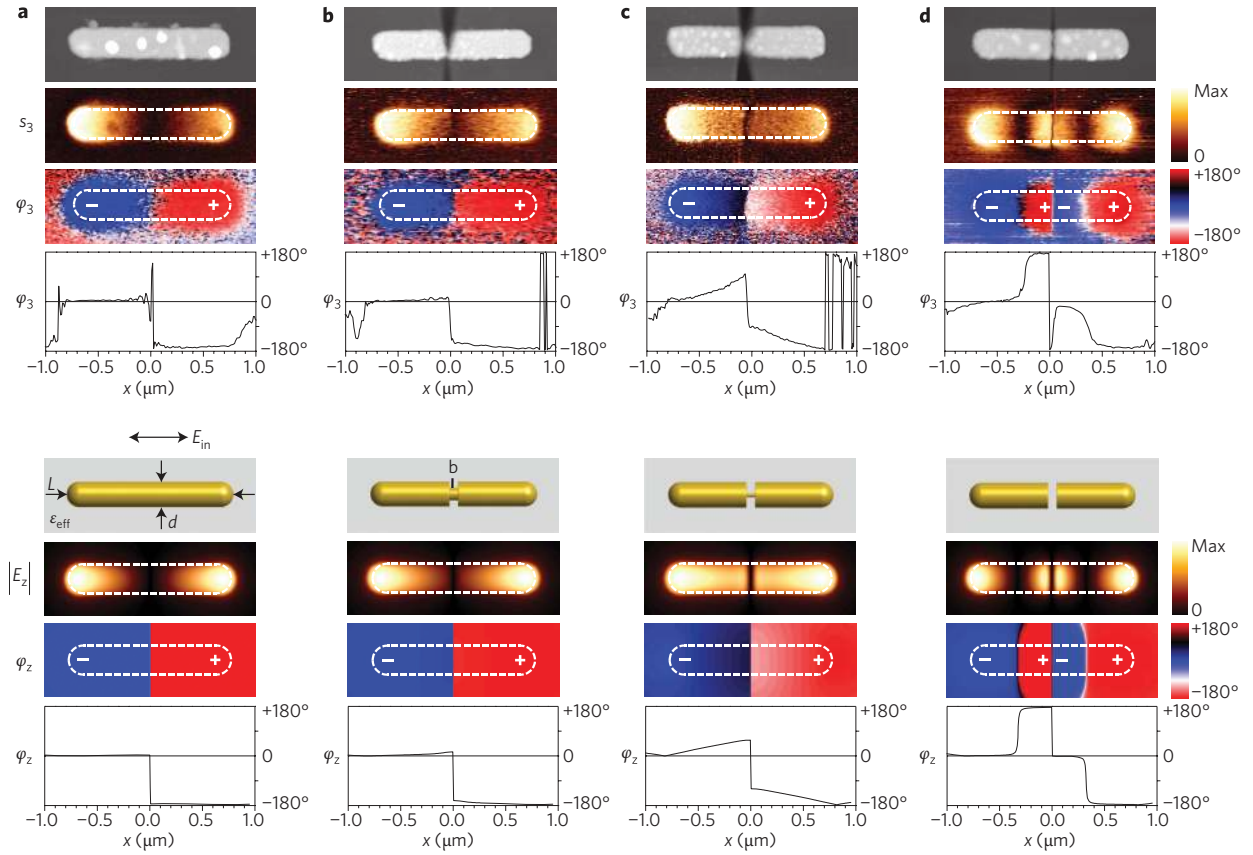

Figure 2 | Near-field images of progressively loaded nanoantennas at a wavelength of $\lambda = 9.6$ μm. a, Continuous rod antenna. **b**, Low-impedance loaded antenna where a thick metal bridge connects the two antenna segments. **c**, High-impedance loaded antenna where a tiny metal bridge connects the two antenna segments. **d**, Fully cut antenna where the two antenna segments are completely separated. Top: Experimental results showing topography and near-field amplitude s_3 and phase φ_3 images. Bottom: Theoretical near-field distribution of a model system, a 1,550-nm-long gold rod with diameter $d = 230$ nm and an 80-nm gap in its centre, embedded in an effective medium of dielectric value $\varepsilon_{eff} = 6.34$. The gap is bridged by gold disks of 80 nm length with diameters $b = 230$ nm (**a**), $b = 80$ nm (**b**), $b = 40$ nm (amplitude image, **c**) and $b = 30$ nm (phase image, **c**), $b = 0$ nm (**d**). The near-field images show the z-component of the electric field in amplitude E_z and phase φ_z in a height of 50 nm above the rod surface. In all phase images, the phase is set to 0° at the left antenna extremity.

central gap of about 80 nm. The near-field images show that both antenna segments oscillate in a dipolar-like mode, featuring high-amplitude signals at the antenna extremities and near the gap, as well as a phase jump of 180° near the centre of each segment and inside the gap. This is in good agreement with numerical calculations assuming an 80-nm gap in the rod centre (Fig. 2d, bottom).

The near-field patterns of the gap antennas are completely changed when a metal bridge (representing the load) connects the two antenna segments (Fig. 2b). Near the gap, in contrast to the fully cut rod (Fig. 2d), no significant near fields are observed. The topography clearly reveals the deep, wedge-like cut through the rod centre and also shows the metal bridge at the lower rim of the rod. Obviously, the small metal bridge (about 10% of the total cross-section of the nanorod, estimated from the topography) suffices to restore the fundamental dipolar near-field mode of the continuous rod (Fig. 2a). We attribute this effect to a current flow through the bridge that prevents charge pile-up at the gap.

A highly interesting near-field distribution is observed in Fig. 2c where a much thinner metal bridge connects the nanorod segments. The bridge cross-section is estimated from the topography to be about 2% of the total rod cross-section, thus being significantly reduced compared to Fig. 2b. The near-field images show striking differences to both the continuous and fully cut rods. We observe a significant amplitude signal along the total length of each segment and a considerable phase gradient of about 80°. To further illustrate this interesting behaviour, we monitored the near-field oscillations of the antennas in space and time. Owing to the simultaneous acquisition of amplitude $s_3(x, y)$ and phase $\varphi_3(x, y)$ signals, we can represent the near field at a sample position (x, y) and at time t by

$$f(x, y, t) = \mathrm{Re}[s_3(x, y)e^{i\varphi_3(x,y)-i2\pi t/T}] \quad (1)$$

where T is the oscillation period. A series of snapshots of f for all four antennas investigated in this Letter is shown in Fig. 3. For the continuous rod (Fig. 3a, obtained from data in Fig. 2a) the snapshots clearly show the time evolution of a single dipolar oscillation, whereas the result for the fully cut rod (Fig. 3d) reveals two closely spaced dipolar-like modes evolving simultaneously in time. In the case where the tiny metal bridge connects the antenna segments (Fig. 3c), however, we observe a significant time delay between the near fields at the gap and the antenna extremities.

To analyse the near-field behaviour of the metal-loaded antennas (Fig. 2b,c), we calculate the z-component of the near-field amplitude $|E_z|$ and phase φ_z, assuming an 80-nm gap in between the antenna segments, loaded with 80-nm-long cylindrical gold bridges of diameters between $b = 0$ nm and $b = 230$ nm. The results (see Supplementary Fig. S2) reveal that by progressive antenna loading (increasing bridge diameter b) the near-field pattern of the fully

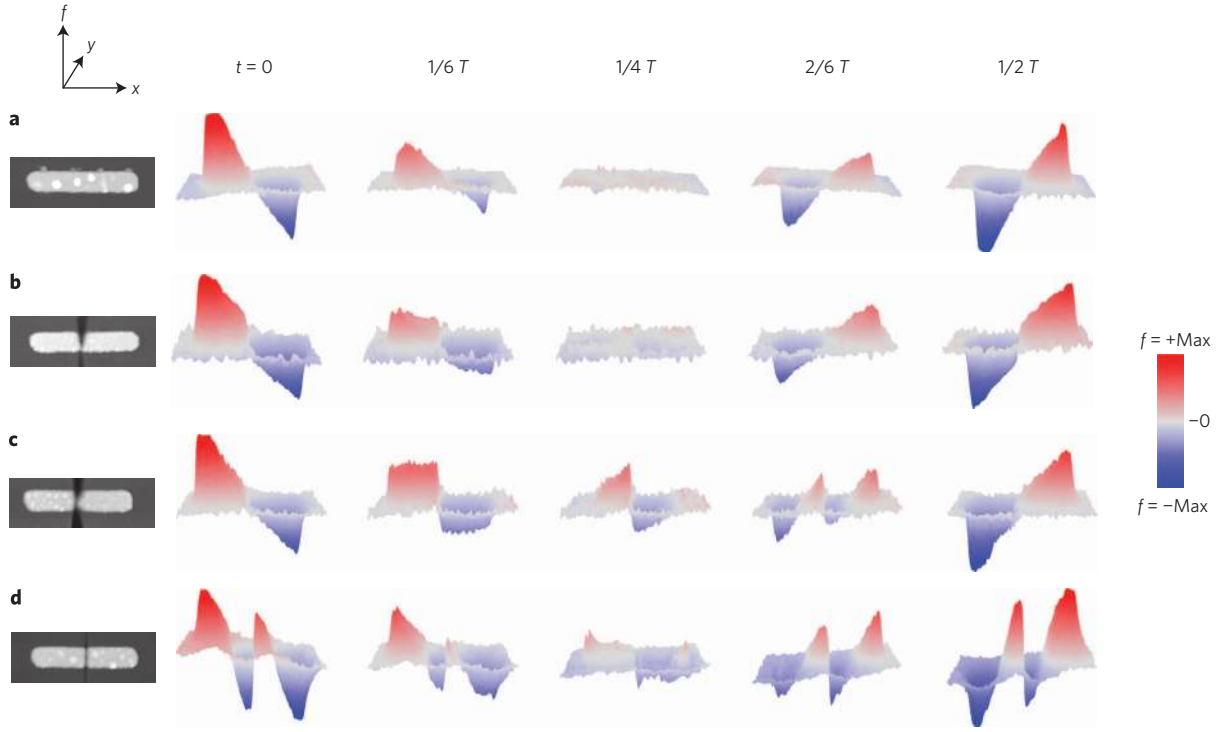

Figure 3 | Time evolution of the antenna's near-field distribution *f* obtained from the experimental data of Fig. 2. a, Continuous rod antenna. **b**, Low-impedance (inductive) loaded antenna (thick metal bridge). **c**, High-impedance (inductive) loaded antenna (tiny metal bridge). **d**, Fully cut antenna. *T* denotes the oscillation period. The corresponding movie of the near-field oscillations is provided in the Supplementary Information.

cut rod ($b = 0$) evolves towards the fundamental dipolar mode of the continuous rod. Comparing experiment and theory, we can assign to each s-SNOM image a calculated near-field pattern. For the antenna in Fig. 2b we obtain good agreement for a bridge diameter $b = 80$ nm, which corresponds to 12% of the rod's cross-section. This is consistent with the bridge size estimated from the topography image. The s-SNOM images in Fig. 2c match well with calculated near-field patterns for b between 30 to 40 nm (~2% of the rod cross-sectional area), thus confirming that indeed a tiny metallic bridge is connecting the two segments in our experiment. It is interesting to note that the variation of the single parameter b is sufficient to reproduce all the experimentally observed near-field patterns (Fig. 2a–d).

To provide further theoretical insights, we calculated the extinction spectra of the gap antennas for bridge diameters between 0 and 100 nm; these are summarized in the contour plot of Fig. 4a. For large bridge diameter b, we observe a first-order dipolar mode (D1) of the antenna at around $\lambda \approx 10$ μm (according to the experimental and theoretical near-field distributions shown in Fig. 2b) and a weaker second-order dipolar mode (D2) at $\lambda = 3.5$ μm. With decreasing bridge diameter b, we observe a slight redshift of both modes. Reaching small bridge diameters $b < 50$ nm, the behaviour changes significantly. The first-order mode (D1) experiences a divergent redshift at $b \approx 20$ nm while being increasingly damped. This can be explained by the restriction of the charge flow across the gap that is necessary to build up a mode structure compatible with D1. Thus, in the limit of very small bridge diameters, the first-order mode (D1) cannot be excited anymore. The second-order mode (D2), in contrast, is enhanced with decreasing b and turns into the first-order mode of the coupled nanorods (C1), owing to the compatible structure of both modes. Considering now the antenna response at the fixed wavelength $\lambda = 9.6$ μm, we clearly observe a transition from the first-order dipolar mode (D1) of a continuous rod (large b) towards the mode of the coupled nanorods (C1) when b is decreasing. At a given bridge diameter of ~30 nm (corresponding to our experimental situation where a tiny bridge connects the antenna gap, Fig. 2c) the antenna response at a wavelength of $\lambda = 9.6$ μm lies in between the two branches coming from D1 and D2. Thus, the near-field distribution of the antenna comprises contributions of both branches, yielding the strong phase shift on each antenna segment, an effect that we clearly identify in both the experimental and calculated near-field images.

In the RF range, circuit theory is an essential tool for the efficient design of antenna devices. Adopting RF concepts, we now show how the behaviour of our loaded infrared antennas can be explained within the framework of optical circuit theory, which has recently been introduced by Engheta and colleagues[9–11]. We can describe the impedance of the antenna load Z_{load} as a parallel circuit composed of the inductive impedance of the metallic bridge Z_{bridge} and the capacitive impedance of the effective medium filling the gap Z_{gap}, given by

$$Z_{\mathrm{bridge}} = \frac{ig}{\omega\varepsilon_{\mathrm{Au}}\pi\left(\frac{b}{2}\right)^2}, \quad Z_{\mathrm{gap}} = \frac{ig}{\omega\varepsilon_{\mathrm{eff}}\pi\left[\left(\frac{d}{2}\right)^2 - \left(\frac{b}{2}\right)^2\right]} \qquad (2)$$

Here, g is the gap width (80 nm), ω the infrared frequency, $\varepsilon_{\mathrm{Au}}$ the dielectric value of gold and $\varepsilon_{\mathrm{eff}}$ the dielectric value of the effective medium filling the gap of our model antennas considered in Figs 2 and 4a. In Fig. 4b we display a contour plot that shows the value of the load reactance X_{load} (given by $Z_{\mathrm{load}} = R_{\mathrm{load}} - iX_{\mathrm{load}}$) as a function of bridge diameter b and wavelength λ, highlighting regions of inductive (blue) and capacitive (red) behaviour. Comparing the evolution of the antenna modes (Fig. 4a) with the behaviour of X_{load} (Fig. 4b), we find an interesting connection: the first-order mode D1 strongly shifts to longer wavelengths when X_{load} increases (more inductive, displayed in darker blue). The region of capacitive X_{load},

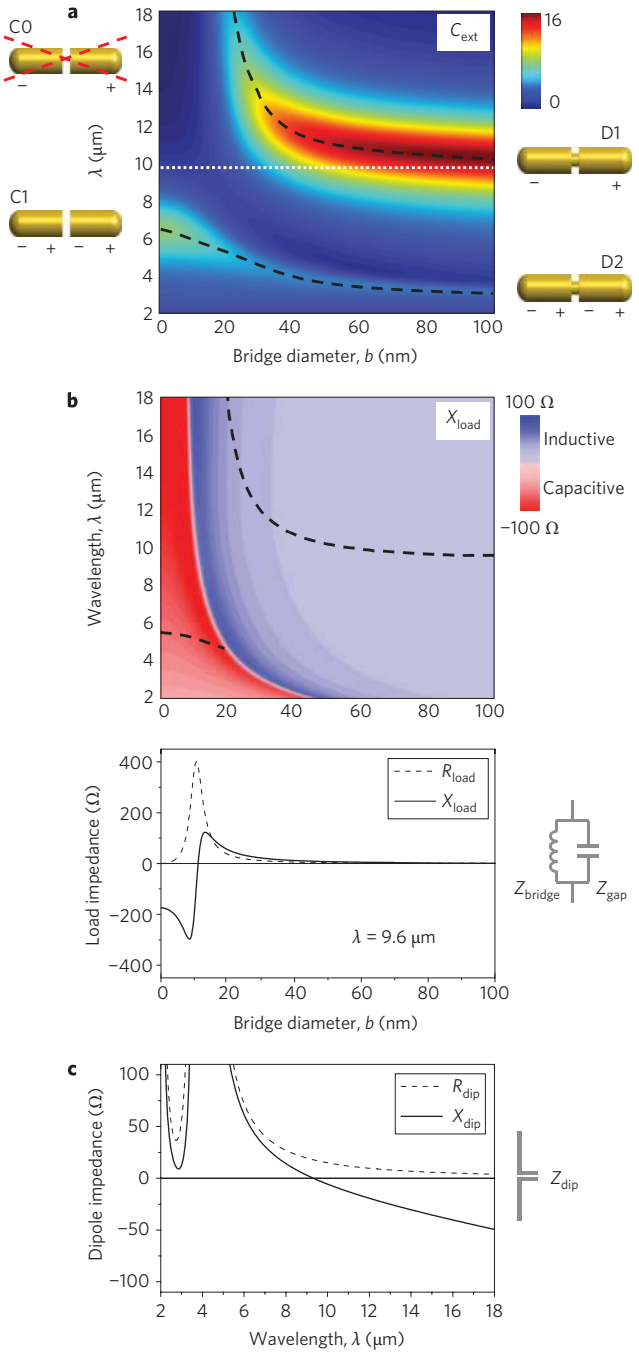

Figure 4 | Comparison of numerical calculations and antenna theory. **a**, Extinction cross-section calculated for the antennas considered in Fig. 2 as a function of the bridge diameter *b*, normalized to the projected area of the antenna. The dashed black lines trace the extinction resonances. The first-order and second-order modes of the continuous rod are marked by D1 and D2, respectively. For antennas with $b = 0$ (isolating gap), C1 is the first-order mode. The zero-order mode C0 is unphysical because it would have finite charge on each antenna segment[22]. **b**, Top: Contour plot displaying the load reactance X_{load} as a function of *b* and wavelength λ. Regions of capacitive reactance (negative X_{load}) are shown in red, regions of inductive reactance (positive X_{load}) in blue. The black dashed lines trace the first-order antenna resonances calculated by means of circuit theory. Bottom: Load resistance R_{load} and load reactance X_{load} displayed as a function of *b*, calculated for $\lambda = 9.6$ μm. **c**, Intrinsic resistance R_{dip} and reactance X_{dip} of a cylindrical dipole antenna as a function of wavelength. The calculation is based on standard equations of antenna theory[30] and assumes a 1,550-nm-long antenna of 230-nm diameter embedded in an effective medium with $\varepsilon_{eff} = 6.34$.

however, does not support the D1 mode. The intensity of the D2 mode in contrast strongly increases when the load becomes mainly capacitive. We can describe the load-induced spectral shifts of the antenna modes by modelling our infrared dipole antennas as a series combination of the dipole intrinsic impedance $Z_{dip} = R_{dip} - iX_{dip}$ (Fig. 4c) and the load impedance Z_{load} (refs 9,10). In this equivalent circuit, the antenna resonance occurs when the load reactance cancels the dipole intrinsic reactance, $X_{load} = -X_{dip}$. Evaluating this condition, we obtain the resonance wavelength as a function of bridge size *b*. The result is shown in Fig. 4b by dashed lines. For large *b*, the circuit resonance appears at a wavelength of ~9.3 μm, which is in good agreement with the resonance wavelength obtained from the extinction spectrum (Fig. 4a). With decreasing *b*, still in the inductive region, we find that the circuit resonance is redshifted owing to an increase of the load reactance X_{load} (darker blue). Below the critical bridge size b_c—which we define as the turning point where the load changes from inductive to capacitive nature—the circuit resonance suffers an abrupt change, shifting to shorter wavelengths owing to the change of sign of X_{load}, and correspondingly of X_{dip}. Comparing the evolution of the circuit resonances (dashed lines in Fig. 4b) with the spectral behaviour of the antenna modes (dashed lines in Fig. 4a), we find a remarkable agreement considering the simplicity of the model based on classical antenna theory. We expect an even better agreement by taking into account plasmonic effects[15] that are already present at infrared frequencies[6,25].

Finally, we address how the role of the load impedance affects the near-field distribution of the antennas. At $\lambda = 9.6$ μm the dipole intrinsic impedance amounts to $Z_{dip} = (17 + 2i)\ \Omega$ (Fig. 4c). For large bridge diameters ($b > 80$ nm) we find that the load impedance Z_{load} is considerably smaller than Z_{dip}, thus facilitating current flow through the load. Consequently, accumulation of charges at the gap is very low, yielding negligible near fields in its vicinity (Fig. 2b). Below the critical bridge size b_c, the load impedance is of capacitive nature. Therefore, charges are piled up at the gap, which generate strong near fields, as observed both in experiment and calculations (Fig. 2d). Interestingly, the deviation of the near-field patterns from dipolar-like modes (Fig. 2c) occurs close to the critical bridge size (see also Supplementary Fig. S2), thus confirming that the change of the near-field distribution is a consequence of the transition from inductive to capacitive load impedance.

In conclusion, the near-field images of gap antennas presented here provide direct experimental evidence that the local near-field amplitude and phase distribution can be controlled by antenna loading. This opens the door for designing near-field patterns without the need to change antenna length, which could be highly valuable for the development of compact and integrated nanophotonic devices.

Methods

Near-field microscopy. Our s-SNOM[21,23] is based on an atomic force microscope (AFM) in which cantilevered tips locally scatter the near fields of the antennas (Fig. 1). Recent s-SNOM studies[24,26–28] of plasmon-resonant nanostructures have shown that dielectric tips and appropriate polarization schemes reduce the tip–sample near-field interaction, allowing for faithful mapping of plasmonic near-field modes. In our setup we thus use silicon tips and illuminate the sample from below (transmission-mode). Owing to weak focusing, the laser beam is polarized parallel to the sample surface with only a negligible component along the tip axis. We thus achieve efficient excitation of the antennas and avoid direct excitation of the tip. Furthermore, the transmission mode offers the advantage of homogeneous antenna illumination, thus avoiding phase-retardation effects[27] inherent to the backscattering geometry in typical s-SNOM experiments.

Imaging of the antennas was performed with a CO_2 laser operating at $\lambda = 9.6$ μm. The polarization of the incident field was adjusted to be parallel to the antenna axis and the polarization of the reference beam was chosen parallel to the tip axis (*z*-axis). The tip-scattered light was collected with a parabolic mirror and recorded simultaneously with topography. Background contributions were suppressed by vertical tip oscillation at frequency Ω and by subsequent higher-harmonic demodulation of the detector signal at $n\Omega$ with $n \geq 2$ (refs 21,24,26,27). In combination with pseudoheterodyne interferometric detection, near-field optical amplitude s_n and phase φ_n images were obtained[23].

Because of the weak scattering efficiency of the silicon tips, we needed to operate with tapping amplitudes of ~200 nm. For such large tapping amplitudes, background contributions were not fully suppressed, even with signal demodulation at $n = 3$. Nevertheless, background-free near-field images could be obtained by complex-valued subtraction of the background contribution because (i) s-SNOM signals obtained by pseudoheterodyne interferometric detection are a linear complex-valued sum of near-field and background contributions[23], and (ii) the background in the presented experiments was found to be constant in the x–y plane.

Numerical calculations. The near-field distribution (Fig. 2) and the extinction cross-section (Fig. 4a) of the antennas were calculated numerically with the boundary element method (BEM)[29]. Note that in the experiment the antenna consisted of flat sections of gold on a silicon substrate, with air above the substrate, whereas the calculations were based on cylindrical rods situated in an effective medium. The dielectric value of the effective medium was chosen such that the resonance of the continuous rod ($b = 230$ nm) matched the experimental resonance measured for the 1,550-nm-long gold nanorod on the silicon substrate[2]. Owing to the presence of the silicon substrate (the effective medium surrounding the antennas in the numerical calculations), the resonance is strongly redshifted when compared to nanorods situated in air[22].

The near-field distributions were calculated for a height of 50 nm above the antenna surface. This value was chosen in order to obtain best agreement between the experimental and numerical near-field patterns for the continuous and the fully cut rods (Fig. 2a,d). Note that in the experiments the bridge dimensions can only be estimated from the topography images. Further, the calculations do not take into account the V-shape of the gap. Both aspects could explain the differences between the theoretical and experimental bridge size for a given near-field pattern. Also, this might be the reason why we find the best agreement for amplitude and phase images for slightly different bridge diameters.

Received 11 November 2008; accepted 11 March 2009; published online 19 April 2009

References

1. Grober, R.-D., Schoellkopf, R.-J. & Prober, D.-E. Optical antenna: Towards a unity efficient near-field optical probe. *Appl. Phys. Lett.* **70,** 1354–1356 (1997).
2. Crozier, K. B., Sundaramurthy, A., Kino, G. S. & Quate, C. F. Optical antennas: Resonators for local field enhancement. *J. Appl. Phys.* **94,** 4632–4642 (2003).
3. Mühlschlegel, P., Eisler, H.-J., Martin, O. J. F., Hecht, B. & Pohl, D. W. Resonant optical antennas. *Science* **308,** 1607–1609 (2005).
4. Schuck, P. J., Fromm, D. P., Sundaramurthy, A., Kino, G. S. & Moerner, W. E. Improving the mismatch between light and nanoscale objects with gold bowtie nanoantennas. *Phys. Rev. Lett.* **94,** 017402 (2005).
5. Taminiau, T. H., Stefani, F. D., Segerink, F. B. & Van Hulst, N. F. Optical antennas direct single-molecule emission. *Nature Photon.* **2,** 234–237 (2008).
6. Neubrech, F. *et al.* Resonant plasmonic and vibrational coupling in a tailored nanoantenna for infrared detection. *Phys. Rev. Lett.* **101,** 157403 (2008).
7. Tang, L. *et al.* Nanometre-scale germanium photodetector enhanced by a near-infrared dipole antenna. *Nature Photon.* **2,** 226–229 (2008).
8. Xu, H., Bjerneld, E. J., Käll, M. & Börjesson, L. Spectroscopy of single hemoglobin molecules by surface enhanced raman scattering. *Phys. Rev. Lett.* **83,** 4357–4360 (1999).
9. Alu, A. & Engheta, N. Input impedance, nanocircuit loading and radiation tuning of optical nanoantennas. *Phys. Rev. Lett.* **101,** 043901 (2008).
10. Alu, A. & Engheta, N. Tuning the scattering response of optical nanoantennas with nanocircuit loads. *Nature Photon.* **2,** 307–310 (2008).
11. Engheta, N., Salandrino, A. & Alu, A. Circuit elements at optical frequencies: Nanoinductors, nanocapacitors and nanoresistors. *Phys. Rev. Lett.* **95,** 095504 (2005).
12. Stockmann, M. I., Faleev, S. V. & Bergmann, D. J. Coherent control of femtosecond energy localization in nanosystems. *Phys. Rev. Lett.* **88,** 67402 (2002).
13. Aeschlimann, M. *et al.* Adaptive subwavelength control of nano-optical fields. *Nature* **446,** 301–304 (2007).
14. Shalaev, V. M. Optical negative-index metamaterials. *Nature Photon.* **1,** 41–48 (2007).
15. Novotny, L. Effective wavelength scaling for optical antennas. *Phys. Rev. Lett.* **98,** 266802 (2007).
16. Kim, S. *et al.* High-harmonic generation by resonant plasmon field enhancement. *Nature* **453,** 757–760 (2008).
17. Ghenuche, P., Cherukulappurath, S., Taminiau, T. H., Van Hulst, N. F. & Quidant, R. Spectroscopic mode mapping of resonant plasmon nanoantennas. *Phys. Rev. Lett.* **101,** 116805 (2008).
18. Atay, T., Song, J. H. & Nurmikko, A. V. Strongly interacting plasmon nanoparticle pairs: From dipole–dipole interaction to conductively coupled regime. *Nano Lett.* **4,** 1627–1631 (2004).
19. Romero, I., Aizpurua, J., Bryant, G. W. & de Abajo, F. J. G. Plasmons in nearly touching metallic nanoparticles: singular response in the limit of touching dimers. *Opt. Express* **14,** 9988–9999 (2006).
20. Lassiter, J. B. *et al.* Close encounters between two nanoshells. *Nano Lett.* **8,** 1212–1218 (2008).
21. Keilmann, F. & Hillenbrand, R. Near-field optical microscopy by elastic light scattering from a tip. *Philos. Trans. R. Soc. London, Ser. A* **362,** 787–805 (2004).
22. Aizpurua, J. *et al.* Optical properties of coupled metallic nanorods for field-enhanced spectroscopy. *Phys. Rev. B* **71,** 235420 (2005).
23. Ocelic, N., Huber, A. & Hillenbrand, R. Pseudoheterodyne detection for background-free near-field spectroscopy. *Appl. Phys. Lett.* **89,** 101124 (2006).
24. Olmon, R. L., Krenz, P. M., Jones, A. C., Boreman, G. D. & Raschke, M. B. Near-field imaging of optical antenna modes in the mid-infrared. *Opt. Express* **16,** 20295–20305 (2008).
25. Fumeaux, C. *et al.* Measurement of the resonant lengths of infrared dipole antennas. *Infrared Phys. & Technol.* **41,** 271–281 (2000).
26. Hillenbrand, R., Keilmann, F., Hanarp, P., Sutherland, D. S. & Aizpurua, J. Coherent imaging of nanoscale plasmon patterns with a carbon nanotube optical probe. *Appl. Phys. Lett.* **83,** 368–370 (2003).
27. Esteban, R. *et al.* Direct near-field optical imaging of higher order plasmonic resonances. *Nano Lett.* **8,** 3155–3159 (2008).
28. Yu, N. *et al.* Plasmonic quantum cascade laser antenna. *Appl. Phys. Lett.* **91,** 173113 (2007).
29. Garcia de Abajo, F. J. & Howie, A. Relativistic electron energy loss and electron-induced photon emission in inhomogeneous dielectrics. *Phys. Rev. Lett.* **80,** 5180–5183 (1998).
30. Balanis, C. A. *Antenna Theory* (John Wiley & Sons, 2005).

Acknowledgements

The authors would like to thank A. Ziegler and A. Rigort (both Abteilung Molekulare Strukturbiologie, Max-Planck-Institut für Biochemie) for help with FIB milling and M. Raschke (Seattle) and N. Engheta (University of Pennsylvania) for stimulating discussions. We thank Nanosensors (Erlangen) for providing HF-etched silicon tips, F.J. García de Abajo for BEM tools and C.F. Quate and G.S. Kino (both Stanford University) for previous insights on the optical antennas studied in this Letter. This research was supported by the Etortek program of the Department of Industry of the Basque Government and the Basque Foundation for Science (Ikerbasque). J.A. acknowledges CSIC special intramural project PIE 2008601039.

Additional information

Supplementary information accompanies this paper at www.nature.com/naturephotonics. Reprints and permission information is available online at http://npg.nature.com/reprintsandpermissions/. Correspondence and requests for materials should be addressed to R.H.